Deciphering the Atomic Scale Electrocatalytic Sites in Hierarchically Porous Gold Nanostructures: Implications for Ascorbic Acid Electrooxidation

Abhishek Kumar, Johann Lüder, Mauro Bertotti, Koiti Araki, Fabiano Montoro, Frederic Herbst, Rita Meunier-Prest, Lucio Angnes, Marcel Bouvet, Jefferson Bettini, et al.

To cite this version:

Abhishek Kumar, Johann Lüder, Mauro Bertotti, Koiti Araki, Fabiano Montoro, et al.. Deciphering the Atomic Scale Electrocatalytic Sites in Hierarchically Porous Gold Nanostructures: Implications for Ascorbic Acid Electrooxidation. ACS Applied Nano Materials, 2024, 7 (7), pp.7213 - 7225. ⟨10.1021/acsanm.3c06226⟩. ⟨hal-04611966⟩

HAL Id: hal-04611966
https://hal.science/hal-04611966v1

Submitted on 14 Jun 2024

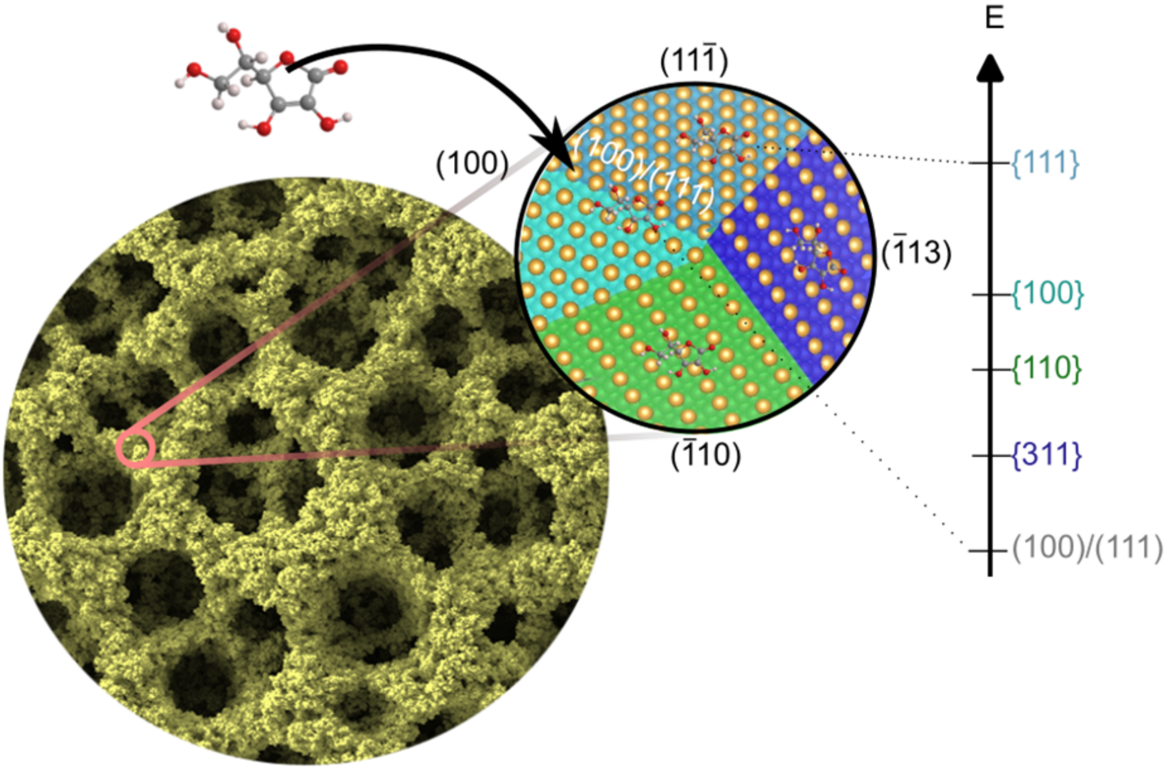
(11$\bar{1}$)
(100)
(100)/(111)
($\bar{1}$13)
($\bar{1}$10)
E
{111}
{100}
{110}
{311}
(100)/(111)

Deciphering the Atomic Scale Electrocatalytic Sites in Hierarchically Porous Gold Nanostructures: Implications for Ascorbic Acid Electrooxidation

Abhishek Kumar[1,2]*, Johann Lüder[3,4,5]*, Mauro Bertotti[2], Koiti Araki[2], Fabiano Montoro[6], Frederic Herbst[7], Rita Meunier-Prest[1], Lucio Angnes[2], Marcel Bouvet[1], Jefferson Bettini[6], Josue M. Gonçalves[2]*

[1]*Institut de Chimie Moléculaire de l'Université de Bourgogne, UMR CNRS 6302, Université Bourgogne Franche-Comté, Dijon, France*

[2]*Department of Fundamental Chemistry, Institute of Chemistry, University of São Paulo, Av. Prof. Lineu Prestes, 748, 05508-000 São Paulo, SP, Brazil*

[3]*Department of Materials and Optoelectronic Science, National Sun Yat-sen University, Kaohsiung 80424, Taiwan*

[4]*Center for Theoretical and Computational Physics, National Sun Yat-sen University,*

Kaohsiung 80424, Taiwan

[5]*Center of Crystal Research, National Sun Yat-sen University, Kaohsiung 80424, Taiwan*

[6]*LNNano—Brazilian Nanotechnology National Laboratory—CNPEM, R. Giuseppe Máximo Scolfaro, 10000—Polo II de Alta Tecnologia, 13083-970 Campinas, SP, Brazil*

[7]*Laboratoire Interdisciplinaire Carnot de Bourgogne (LICB), UMR CNRS 6303, Université de Bourgogne, 9 avenue Alain Savary, 21078 Dijon cedex, France*

Email addresses and ORCID number of authors (corresponding authors emails are marked with asterisk)

*abhishek.Kumar@u-bourgogne.fr (ORCID no. 0000-0002-4306-9644)
*johann.lueder@mail.nsysu.edu.tw (ORCID no. 0000-0001-6603-8376)
mbertott@iq.usp.br (ORCID no. 0000-0001-9566-7577)
koiaraki@iq.usp.br (ORCID no. 0000-0003-3485-4592)
fabiano.montoro@lnnano.cnpem.br
frederic.herbst@u-bourgogne.fr (ORCID no. 0000-0002-7774-4433)
rita.Meunier-Prest@u-bourgogne.fr (ORCID no. 0000-0001-5597-3879)
luangnes@iq.usp.br (ORCID no. 0000-0003-3639-6783)
marcel.bouvet@u-bourgogne.fr (ORCID no. 0000-0002-2272-6633)
jefferson.bettini@lnnano.cnpem.br
*josuefisicoquimico@hotmail.com (ORCID no. 0000-0003-0800-077X)

Abstract: Understanding the structure and origin of catalytic sites at the nanometer/sub-nanometer scale in porous nanomaterials is essential for an efficient and durable catalyst design. Herein, chemically pure nanoporous gold (NPG) having a hierarchically porous network is electrochemically synthesized, and its microstructure is investigated by electron microscopies, electrochemical methods and ab-initio simulations to unravel the identification of catalytic sites for ascorbic acid (AA) electrochemical oxidation. Experimental characterizations reveal a highly porous NPG film, containing polycrystalline and interconnected dendrite fractals. The film growth follows a unique pattern such that at the beginning of the film growth, Au grains are smaller, which at the later growth stage become larger and expose low-index facets and structural defects, such as dislocation of Au atoms, atomic steps, and kinks. Such structural defects and facets evolutions in the NPG film cause a remarkable electrocatalytic effect towards the electrochemical oxidation of AA, which is interpreted based on Density Function Theory (DFT) simulation. The simulation predicts stronger binding of AA on the low-indexed Au facets and grain boundaries, leading to larger electronic charge transfer from AA to the Au atoms. In particular, grain boundary regions provide vacancy-like sites, in which part of AA locks itself, forming a stronger bond with Au atom of partial covalent character. The low catalytic activity of the thermodynamically stable (111) facet is assigned to its flat topography over which AA interacts through mainly van der Waals forces, causing a weaker binding.

Keywords: Nanoporous gold, electrocatalysis, electron microscopies, DFT simulations, molecular dynamics

1. Introduction

The catalysis of oxidation reactions on the gold surface has been an area of intensive study, even though the chemisorption of oxygen on gold is an endothermic process [1]. Researchers have attributed multiple reasons, among which the nanostructuration of Au and the role of metal oxide support have been extensively debated, drastically reducing the nobility of gold and turning it into an efficient and selective catalytic material [2-3]. Nonetheless, intrinsic catalytic properties of Au must be attributed to emanating from nanostructuration, generating unique morphology, uncoordinated surface sites, and reactive structural defects [4-6]. Nanoporous gold (NPG) is an important example of Au nanostructuration, and has been used for different catalytic applications [7], such as selective oxidation of primary alcohols [8], olefins [9] and carbon monoxide [10]. NPG were also used for electrochemical sensing of many environmentally and biochemically relevant species, such as ascorbic acid, dopamine, glucose, nitrite, aptamer-based sensing in living cells among others [11-15]. NPG materials are characterized by a unique monolith of gold, possessing nanometric features of interconnected bicontinuous gold struts and pores, developing sponge-like open-cell morphologies. Such materials were synthesized by chemical and electrochemical methods either through top-down strategies, mainly selective corrosion of gold surfaces or alloys [16-17] and soft-templating[18] or bottom-up protocols, involving electrodeposition from a gold precursor solution [19]. The structure and morphology depend on the choices of the synthesis method adopted. For instance, electrochemical anodic corrosion develops nanoporous morphology of interconnected ligaments and identical pore size, while electrodeposition grows a hierarchically porous structure, possessing a multiplicity of pore sizes and varieties of fractal shapes, depending on the growth conditions [20]. Thus, a large avenue exists to control the nanometric features in NPG by applying synthesis parameters and tuning its catalytic action efficiently. Therefore, NPG materials have presented fascinating structural features extensively studied in many electrochemical applications, further stimulating the research community to explore their intrinsic origin of catalytic properties.

Considerable advances have been made to understand the origin of catalytic properties in unsupported NPG materials [21-25], focusing on the nanoporous geometry, lattice orientation, and atomic scale structural defects. However, nanoporous geometry, which induces the phenomenon of nanoconfinement, is not specific to the intrinsic properties of gold. Instead, it is more of a morphological limitation, enhancing the reaction kinetics of sluggish redox reactions [26-27]. Therefore, the origin of intrinsic catalytic properties of NPG materials must be assigned to the crystallographic orientation and structural defects emanating from the atomic arrangements of gold atoms during synthesis. In NPG materials prepared by selective electrochemical dissolution of less noble metal (Ag or Cu) from a gold-containing alloy, such as Au-Ag or Au-Cu, the origin of structural defects was investigated by many researchers and were mainly assigned to the residual less noble metal impurities trapped in the Au film [28-30]. Indeed, as depicted in the Figure 1a, during selective electrochemical dealloying, most of Ag atoms are selectively etched, however subsequent surface diffusion of Au atoms cluster to form pit-and-mound arrangements, locally passivating the surface and preventing further etching of Ag atoms underneath. The presence of residual Ag atoms in NPG stabilizes the crystalline structural defects of Au, such as terrace, steps and kinks, which have lower coordination number than the bulk gold lattice. These regions act as active sites in the catalytic reactions [28, 31], and further studies elucidated the important role of Ag as a reactive center to adsorb molecular oxygen and its subsequent dissociation to generate atomic oxygen reactive species [32-33], which in turn activates the Au-sites in the electrocatalytic reactions.

Interestingly, pure NPG (absence of less noble metal impurities) prepared by a bottom-up approach, more specifically by Dynamic Hydrogen Bubble Template (DHBT) [34] electrodeposition from gold precursor solution, as shown in Figure 1b, has also exhibited high catalytic activity in oxidation [14, 35-36] and reduction reactions [37]. In the DHBT method, electrochemical deposition of NPG proceeds through synchronous reduction of proton and

Au^{3+}, resulting in the deposition of Au atoms and evolution of H_2 bubbles simultaneously on the electrode, in which the latter provides a dynamic template for the codepositing Au atoms to develop a porous structure. As a result of subsequent nucleation and surface diffusion of the Au atoms [38], the local organizations attain similar pit-and-mound arrangements, as predicted during electrochemical dealloying synthesis of NPG, but remain devoid of any impurities. Therefore, the observed high catalytic properties of such materials in the redox reactions can not be explained by the residual less noble metal atom trapping approach adopted for the NPG prepared by dealloying. It must be other reasons, intrinsic to the atomic arrangements of only gold atoms in the lattice, making DHBT grown NPG film catalytically active in the redox reactions. However, contrary to the multiple studies made to understand the atomic origin of high catalytic properties in NPG prepared by top-down electrochemical dealloying, no such studies have been reported to explain the high intrinsic catalytic activities observed in the NPG prepared by bottom-up DHBT electrodeposition. Thus, our endeavors in the present work are to understand the atomic origin of catalytic properties in pure NPG material.

Herein, we have synthesized NPG material by the DHBT electrodeposition approach and have investigated its structure and the associated atomic scale defects to understand the intrinsic catalytic properties of the material. We have chosen an example of ascorbic acid (AA) as a redox species, which has been shown to undergo an electron transfer coupled chemical reaction in its electrooxidation mechanism. One of the key objectives of the study is to identify subnanometric-size catalytic sites on the NPG surface, which have been investigated by electrochemical methods, in-depth microstructural characterizations by different electron microscopies and ab initio simulations within Density Function Theory (DFT). An emphasis has been given to understand the role of hydrogen bubbles on the microstructural features of NPG, such as grain sizes, grain boundaries, lattice orientations and defects. The electrochemical oxidation of AA on the NPG electrode surface is studied by cyclic voltammetry (CV), and the observed electrocatalysis effect is correlated to the exposed crystal faces, grain size, grain boundaries, and the associated structural defects, deduced from microstructural characterizations. Experimental results are further interpreted by modelling the interaction of AA on different Au facets and grain boundaries by DFT calculations. The simulation explores the multiple adsorption configurations of AA and compute the binding strength on potential sites in different Au planes.

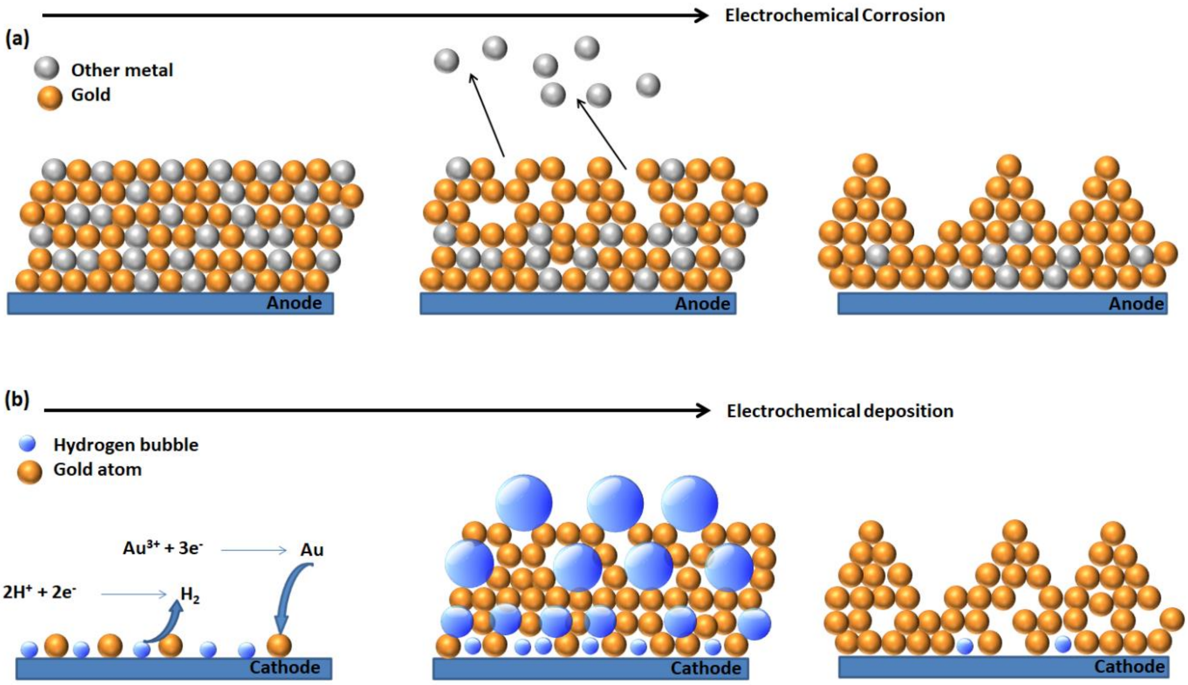

Figure 1: schematic representation of NPG electrosynthesis by electrochemical dealloying (a) and dynamic hydrogen bubble template deposition (b).

2. Experimental details

2.1.Materials and reagents

Analytical grade chemicals were used directly without any further purification in this work. Gold(III) chloride trihydrate, L-ascorbic acid and phosphate buffer (PBS) were purchased from Sigma-Aldrich. PBS buffer solution (pH~7.4) was prepared by dissolving one tablet into 200 mL of deionized water, which was used to prepare the 0.1 M AA stock solution. The 1.6 mm diameter gold disk electrode (from BioLogic) was used in all electrochemical experiments. H_2SO_4 (96.2%) (Merck) was diluted with deionized water to prepare 0.5 M solution.

2.2.Electrochemical setup and preparation of DHBT NPG

The electrochemical measurements were carried out on a PGSTAT-128N and a PGSTAT-320N Autolab potentiostat (Metrohm), utilizing Nova 1.12 software. The experiments were conducted in a three-electrode cell configuration, in which gold disk or NPG coated gold disk, Ag/AgCl (KCl sat.), and a platinum wire were used as working, reference, and auxiliary electrodes, respectively. The bare gold electrode was polished before electrochemical measurements over sandpaper with 0.05 µm alumina particles. The electrochemical studies for AA were performed by cyclic voltammetry (CV) in a argon-saturated and 0.1 M (pH~7.4) PBS solution.

The NPG film was electrodeposited on Au disc electrode by chronoamperometry at a fixed applied potential of -4 V for a deposition time of 100 s in 0.5 M H_2SO_4 solution, containing 5 mM $HAuCl_4$. In order to prevent the formation of large H_2 bubbles on the Au electrode surface during the electrodeposition, the solution was vigorously stirred. The deposited film was washed in distilled water to remove any adsorbed electrolyte species. A voltammogram of the NPG-coated Au electrode was recorded in 0.5 M H_2SO_4 solution in the 0.2–1.6 V potential range at a scan rate of 50 mV s^{-1}.

2.3.Surface and structural characterization

The NPG material was analyzed by XPS using Versaprobe 5000 spectrometer (ULVAC-PHI apparatus), utilizing a monochromatic and focused Al Kα X-ray source (1486.6 eV), to confirm the absence of other elements but gold, by setting the spot size to 200 µm and pass energies to 187.5 eV. A Quanta FEG 650 scanning electron microscope operating at an accelerating voltage of 20 kV was used to study the surface morphologies at low magnification. High magnification images of NPG film were recorded using Hitachi UHR FE-SEM (SE8200) in a high angle (HA) backscattered electron (BSE) detection mode at top detector configuration and at an accelerating voltage of 3 kV.

The cross-section of NPG film was imaged by a transmission electron microscope (JEOL JEM-2100), operating at 200 kV and equipped with a Field Emission Gun (FEG, ZrO/W(100) Schottky field emission electron source). The resolution of the TEM set up was 0.19 nm (point-to-point). The sample preparation for TEM imaging involves several steps. At first, the NPG film was removed from the Au electrode by sonicating in an ultrasonic bath. The isolated NPG is mixed into a PELCO 12 Eponate resin, which is then cured for 24 hours at 60 °C, solidifying the mixture. A RMC PowerTome XL ultramicrotome, equipped with a PELCO diamond knife is used to cut 30 nm thin slice from the solid resin-NPG mixture. The isolated thin slice is transferred onto TEM copper grids (TedPella) for imaging. A similar specimen preparation procedure was followed for transmission Kikuchi diffraction (TKD) measurements on a dual beam microscope, FEI^{TM} Helios and an Oxford Instruments^{TM} Nordlys Max2 EBSD Detector. The TKD analyses were conducted with the samples tilted at an angle of 10 degrees and using a 30 kV electron beam, allowing for the mapping of the material's crystalline structure with a resolution below 10 nm.

2.4. Computational details

Ab initio simulations were performed within the Kohn-Sham Density Functional Theory (DFT) [39-40] with the Quantum Espresso package [41]. In the simulation, the projector augmented wave (PAW) method with kinetic energy cutoff of 560 eV and the Perdew-Burke-Ernzerhof (PBE) [42] exchange-correlation function were used. Atomistic models of the molecule-surface interface allowed us to investigate the adsorbate interaction with different facets of monocrystalline Au surfaces, including Au(100), Au(110), Au(111), and Au(311). Furthermore, we consider grain interface between Au(100) and Au(111) to estimate the impact of Au surface defects on the adsorption mechanism of redox specie. To account for possible weak binding interactions between molecules and the different Au facets, we include the dispersion correction developed by Grimme [43].

The lattice constant of Au was set to 4.10 Å, as reported previously in our computational study [44], which is an acceptable reproduction of the experimental lattice constant (4.08 Å).The simulations included a vacuum region of at least 12 Å in the adsorption direction. Each metal substrate included at least three atomic layers, of which the top two layers were allowed to fully relax during structural relaxations. Single-molecule adsorption of L-ascorbic acid was modeled with lateral sizes of the simulations cells of (100): 19.8×19.8 Å^2, (110): 20.0×19.8 Å^2, (111): 19.8×17.2 Å^2, (111)/(100): 21.4×20.5 Å^2, which ensures minimal interactions of L-ascorbic acid having an extension of about 7 Å with its periodic images. The self-consistent cycles were performed with a kinetic energy cutoff of 560 eV and a sampling of the Brillouin zone at the Γ point was done until energy convergence of 1.6 10^{-4} eV was reached. Structural relaxation continued until all forces on nuclei were less than 0.02 eV / Å.

We distinguish the adsorption distance (d_{ad}), the smallest distance between the atomic center of the molecule and the surface, from the adsorption height (h), which is the vertical projection of the distance between the molecule and the surface. Furthermore, the discussion includes the adsorption distance (d) between only the C/O and Au atoms. The total energy difference between the surface with adsorbate ($E_{surf/mol}$) and the pristine surface (E_{surf}) and the isolated molecule (E_{mol}) defines the adsorption energy E_{ad} , i.e.,

$$E_{ad} = E_{surf/mol} - (E_{surf} - E_{mol})$$

The interaction between the Au surfaces and the molecule was examined with charge density redistributions through charge density differences given as

$$\Delta\rho = \rho_{surf/mol} - (\rho_{surf} - \rho_{mol})$$

where $\rho_{surf/mol}$, ρ_{surf}, and ρ_{mol} are the electronic charge densities $\rho = \rho(x,y,z)$ of the molecule-surface, surface, and molecule calculations, respectively.

3. Results and discussions

3.1. Electrochemical and morphological characteristics

A facile and rapid method to confirm the formation of NPG is to record a CV in an acidic solution, such as 0.5 M H_2SO_4, and compare it with a similar CV recorded using a bare gold electrode. Figure 2a depicts the voltammogram of NPG, exhibiting three oxidation peaks in the scan to positive potential values, characteristic of the oxidation of gold into gold oxide at different crystal faces exposed to the solution interface [45]. On the contrary, the bare gold substrate (CV in the inset of Figure 2a) reveals a single broad oxidation peak corresponding to the gold oxide formation at the mainly thermodynamically stable (111) crystal facet exposed to the solution interface. The evolution of additional (100) and (110) low-index crystal faces in the NPG film is indicative of the growth of a polycrystalline gold structure, and this is attributed to the faster kinetics of Au^{3+} reduction and its arrival at the nucleation center compared to the rate of crystallization of Au atoms in its lattice structure post-deposition [38, 46]. The single large reduction peak in the reverse scan, at around 0.9 V, is assigned to the regeneration of metallic gold from the gold oxide formed in the preceding scan. Notably, the area under the reduction peak in the NPG voltammogram is ca. 800 times higher than that of bare gold, highlighting the remarkable enhancement of the electrochemical active surface area (ECSA) of the NPG film because of the nanostructuration. The ECSA of the NPG film is quantitatively determined as 4.25 cm^2 (Figure S1) and details of the calculation are described in the supporting information. The polycrystalline nature of the NPG film is confirmed in the XRD measurements, exhibiting the diffraction peaks associated to (111), (100) and (110) planes of gold (Figure S2).

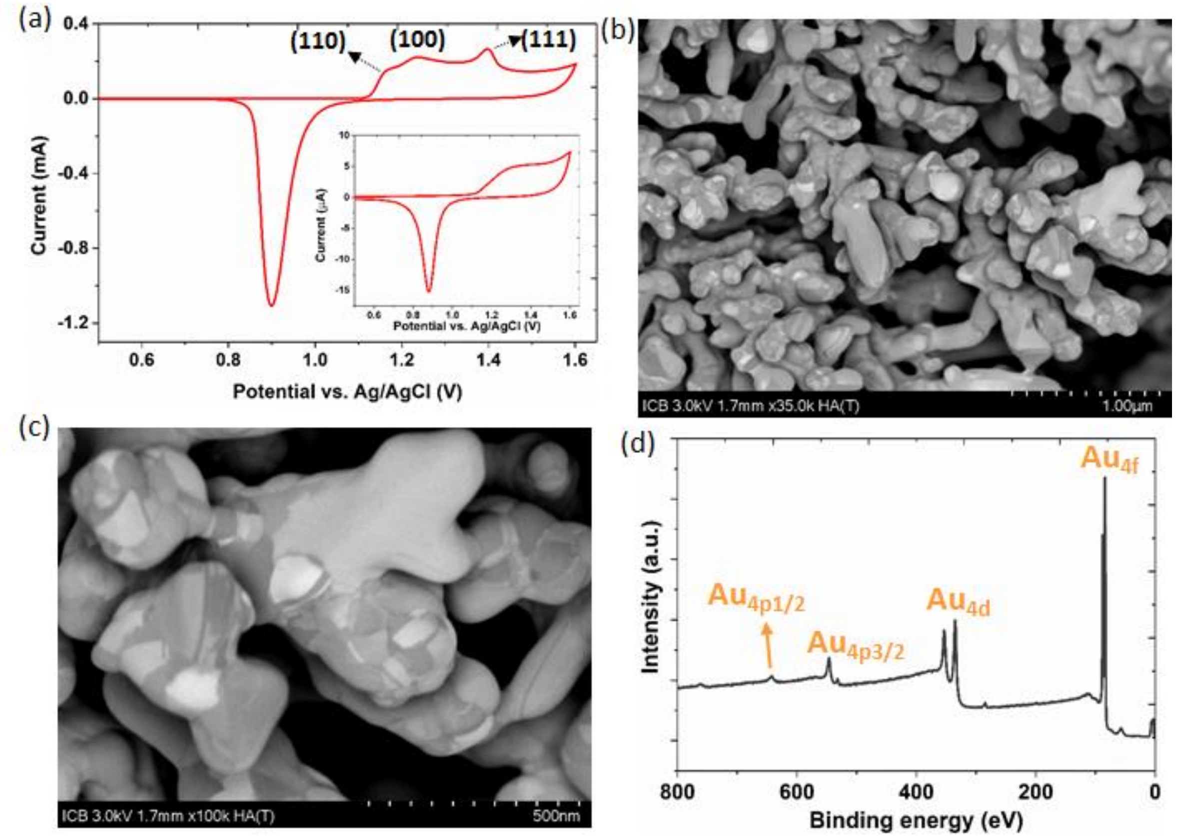

Figure 2: Voltammogram of the NPG electrode recorded in 0.5 M H_2SO_4 solution at the scan rate of 50 mV s^{-1} (a). A similar CV of a bare gold electrode in the same medium is given in the inset. SEM images of an NPG film recorded in HA-BSE imaging mode (b and c). Survey XPS spectrum of the NPG film and its indexing with different Au valence states (d).

To further validate the polycrystalline nature of the NPG film and to investigate its morphology at the same time, the film was imaged with SEM in high angle (HA) backscattered electron (BSE) detection mode at low accelerating voltage (3 kV). In this mode, the backscattered electrons are collected at the top detector of the microscope at a high angle, providing a sharp channeling contrast if there is a change in the lattice orientation, or dislocation defects are present. Accordingly, the backscattered electrons induce a contrast near the crystal boundaries and the edge of the dislocation. Thus, this mode of SEM imaging can reveal crystal orientation and structural defect information on the NPG film surface. Figures 2b and 2c show the SEM micrographs of the NPG film recorded at different magnifications in HA BSE mode. In the low magnification image (Fig. 2b), the morphology is characterized by the growing 3D dendrites fractal and pores of multiple sizes, which are characteristics of the metal film grown by the DHBT method. Besides this, varying degrees of color shading or brightness can be found on the dendrite fractals, and this is indicative of the distribution of different crystal orientations of gold and any possible structural defects. The distribution of different brightness patterns is more evident in the magnified image in Fig. 2c. It is noticed that within the same branch of the dendrite, there are different brightness patterns of varying sizes, which are commensurate with the polycrystalline nature of the branch having different sizes of grains. Moreover, some dendrite branches are monocrystalline, indicated by the unique brightness distributed over a few hundred nm. Thus, SEM imaging further validates the outcome of the electrochemical characterization of NPG film. On a micrometric scale, DHBT-grown film presents a characteristic honeycomb morphology, which is indeed observed for the NPG film (Figure S3), containing surface pores in the range of 10 to 20 µm.

The HA BSE imaging mode of SEM is sensitive to surface impurities, as any compositional differences (atomic number change) can also show variations in the image's brightness. To confirm that there is no surface contamination in the NPG film, it was characterized by XPS, a surface-sensitive technique that can reveal surface impurities. The survey XPS spectrum, as shown in Figure 2d, reveals peaks at 84, 335.2, 353.6, 546, and 642.4 eV, which are associated with the electronic emission from various shells of gold, confirming the high purity of the NPG surface. It also validates that different brightness pattern observed in the SEM image corresponds to the multiple crystalline phases or structural defects of gold. High resolution XPS spectra of Au 4f was recorded and is presented in Figure S4. The spectrum exhibits the two characteristic peaks at 84 eV and 87.7 eV, which corresponds to elemental gold (in zero oxidation state). The separation of ~ 3.7 eV between the $4f_{5/2}$ and $4f_{7/2}$ peaks further validate this. The deconvolution of the spectrum could not show any contribution at 85.6 and 89.1 eV, which are characteristic of Au^+ [47].

3.2.Crystal orientations and structural defects distribution in NPG

Although SEM imaging in HA BSE mode can provide information regarding the polycrystalline nature of the NPG film, but cannot identify the crystal planes and differentiate them with the structural defects. These are important parameters to know because electrochemical reactions are specific to crystal facets exposure and type of defects. Moreover, the distribution of the crystal grains and structural defects within the interior volume of the NPG film is important to characterize because they can influence electrochemical reactions when there is efficient mass transport of redox species within the porous film. Additionally, spatial resolution in HA BSE imaging mode is limited and can not detect precisely the smaller grains and their boundaries below 100 nm. In order to identify the Au crystal facets and see their distribution pattern within the cross-section of the NPG film, a 30 nm thick slice of NPG was cut and was imaged through TKD or t-EBSD method. The key advantage of TKD over the conventional EBSD is that because of the electron transparent thin sample, the electron beam is transmitted and is scattered in the forward direction, enhancing the spatial resolution of the image. At first, thin slice specimen of the NPG film was imaged to validate the cut precision and to select the region of interest (ROI) for the TKD measurement. The image is depicted in Figure 3a, showing a cross-section of the NPG film. Based on this image, a square zone of dimension 2.5 µm × 2.5 µm was chosen as ROI in the specimen for TKD mapping. In the ROI zone, Kikuchi diffraction pattern were recorded in a step size of 7 nm and were presented in Inverse Pole Figure (IPF) in y-axis of visualization. For each pixel in the ROI, the associated IPF gives a unique color point, corresponding to a particular gold crystal orientation, which are identified by the color key indicated in upper right part of Fig. 3. Association of such points for each pixel within the ROI generates the crystal orientation map, which are depicted in Figures 3b. In the image, each color corresponds to Au grains of specific crystal orientation, which can be identified by the triangular color scheme. It has to be noted that the critical misorientation angle is chosen as 10°, which also implies the minimum inclination angle between the neighboring grains at the grain boundaries and the maximum divergence in the orientation within a single grain. The presence of different orientations of Au grains validates its polycrystalline nature within the interior volume of NPG film.

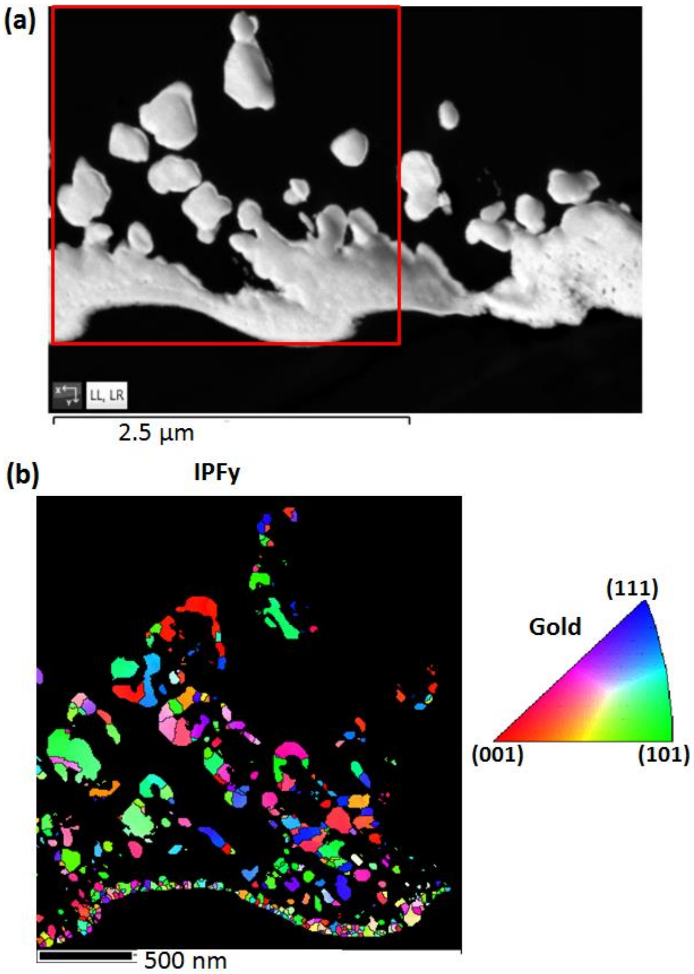

Figure 3: SEM image of a 30 nm slice of an NPG sample recorded in FSD mode (a). IPF crystal orientation map recorded within the selected region of the sample with reference to viewing the direction along y axis (b). The color key of the IPF of gold is indicated on the right side in the lower panel for gold. The critical misorientation angle is 10°.

Notably, the grains are very small, and the NPG film is highly polycrystalline near the substrate or at the beginning of the film growth, while grains become bigger in size far from the substrate or at the later stage of the film growth. Thus, grains are much bigger near the surface of the NPG film. These findings explain the high catalytic activity of NPG towards certain redox reactions because redox species preferentially interact on specific plane/planes and grain boundaries [48-49]. Such variation in the grain sizes within the NPG film is attributed to the fast kinetics of the H_2 evolution reaction near the electrode surface, resulting in vigorous generation of bubbles, impeding the crystallization of Au atoms at the nucleation center. The number of bubbles and their kinetic energy decrease in the direction away from the substrate, allowing a more extended time for crystallization of Au atoms around a nucleation center. To verify the reproducibility of such a growth pattern, a 30 nm thin slice was cut from a different region of NPG film and investigated similarly by TKD. The images in Figure S5 revealed a similar pattern of Au grain's growth. The maps also show the zone´s distribution with high dislocations or structural defects. The grains with corresponding color resembling either extremity of the triangular color key have low structural defects, while those having a color in between contain significant structural defects. It is evident in the maps that there are many regions near the surface of the NPG film possessing a high density of structural defects. Such structural defects were assigned important active sites in the electrocatalytic reactions on NPG film prepared by dealloying [21]. Thus, the orientation map confirms that, even in the absence of residual less noble metal atoms trapped within the NPG film, structural defects are created.

A more precise visualization of the grains rich in structural defects was made by characterizing the crystallographic orientation variation within each grain, commonly called grain orientation spread (GOS). It is computed by estimating the orientation change at each pixel within the grain from the average orientation of the grain, and it is related to the deformation and strain in the grain. For the NPG specimen, GOS was computed for each grain and color-coded depending on its magnitude within the chosen ROI. A light green and yellow color characterizes the higher GOS. At the same time, dark blue represents low GOS (Figure 4a). Notably, most of the smaller grains in the specimen have low GOS. In contrast, a significant number of larger grains revealed GOS higher than 1° (Figure 4b). Thus, grains with higher GOS values have significant lattice distortion caused by different types of structural defects. Additionally, it can be remarked that most of the structural defects containing grains are situated near the surface of the NPG film. It further explains the high catalytic activity of the materials in the electrochemical reactions, as the interaction of the redox active species preferentially takes place near the surface. The grain boundaries and intra-grain misorientation have strong consequences on the strain developed in the NPG film. The strain contour recorded for the same ROI of the NPG film displays distribution of surface strain (Figure S6). Indeed, the strain is higher at the grain boundaries and in the grains with larger GOS. Notably, some of the Au grain with low GOS also exhibited higher strain, which can be assigned to the local environment.

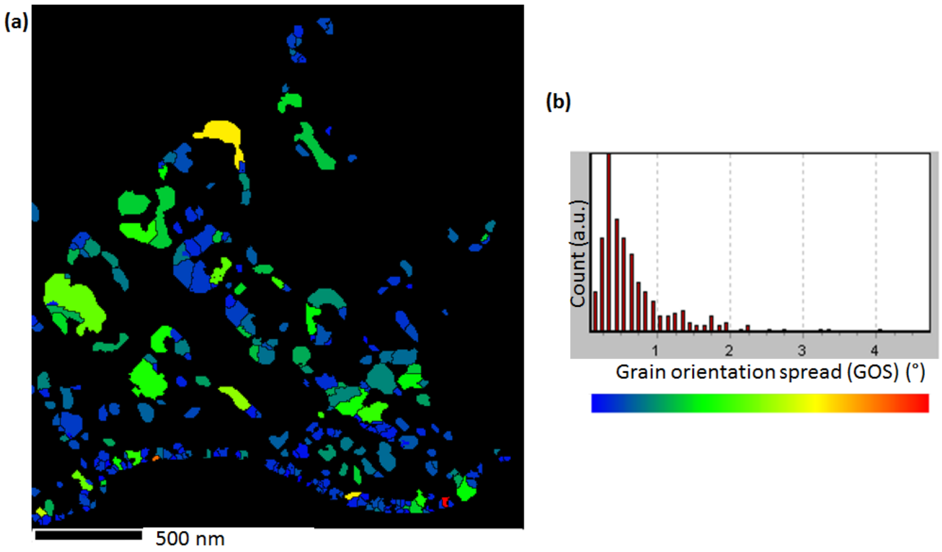

Figure 4: Grain orientation spread (GOS) map (a) and the corresponding statistical distribution (b) generated by the TKD mapping of 30 nm thin film of NPG.

The structural defects and grain orientation pattern during the NPG film growth were further analyzed by HRTEM, as TKD spatial resolution is limited to a few nm. However, HRTEM can provide direct visualization of structural defects and growth patterns with resolution down to atomic scale. The change in the orientation pattern with increasing NPG film thickness was investigated by the selected area electron diffraction (SAED) method in TEM imaging by choosing two different regions (marked as 1 and 2 in Figure 5a) in a 30 nm thin slice of the NPG film. The corresponding diffraction patterns of the two regions are depicted in Figure 5b and 5c. It is clearly observed that the SAED pattern associated with an area away from the bottom of the NPG film (1) presents equally spaced diffraction spots arranged in a linear fashion, a characteristic feature of the monocrystalline orientation of the selected region. On the other hand, the SAED pattern of region 2, located near the bottom of the NPG film, reveals diffraction points arranged in a concentric circle fashion, which indicates a polycrystalline nature of the selected region. Each circle corresponds to a crystal plane of gold, whose diameter is related to the interplanar distance (d-spacing). Thus, the orientation analysis by SAED pattern further provides evidence of monocrystalline grain formation in the later stage of NPG film growth and validates the outcome of the TKD mapping.

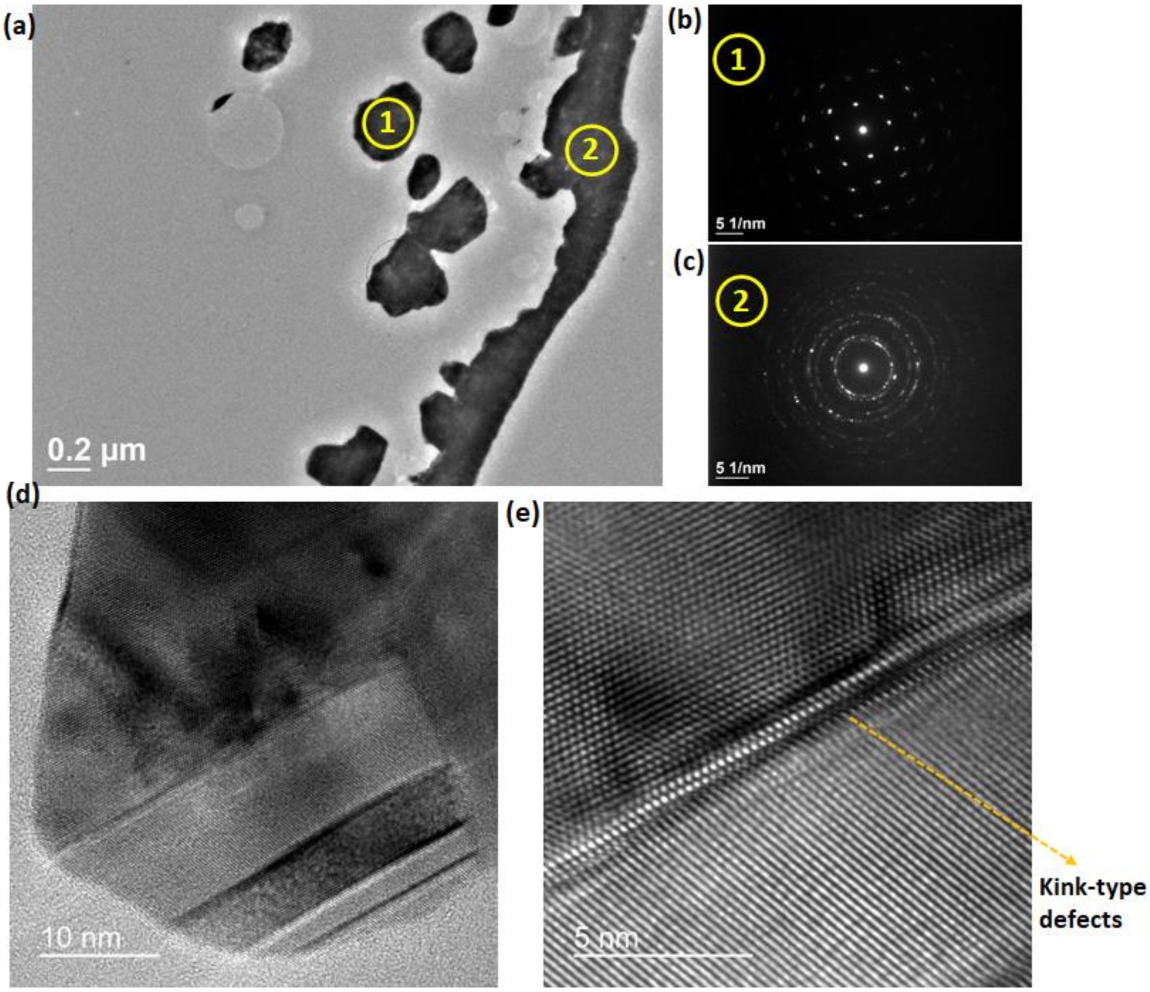

Figure 5. TEM image of a 30 nm thin slice of an NPG film, in which two regions are marked for analysis (a). SAED patterns of region 1 (b) and region 2 (c), marked in the image (a). HRTEM images of the 30 nm thin slice of the NPG film are shown in (d) and (e).

The high-resolution images acquired by TEM of the NPG film cross-section are depicted in Figure 5d and 5e, showing the arrangement of atomic fringes of Au. Figure 5d reveals that the arrangement of fringe lines is not smooth, highlighting multiple steps and dislocations of Au atoms. Such lattice deformations form the structural defects within the NPG film. Another key type of structural defect is the kink, which is developed at the grain boundaries and is shown for the selected region of Figure 5d in a magnified image in Figure 5e. In the image, it is evident that two sets of fringe lines are perpendicular to each other, which lattice orientations are assigned as (111) and (100), by estimating the average distance between the neighboring fringe lines in each grain, corresponding to the respective d-spacing. Notably, at the grain boundary, the Au-atomic fringes are deformed, forming a wave-like pattern, resulting from the inherent local strain built up. Such lattice distortions are commonly referred to as kink-type structural defects (Fig. It also predicts that grain boundaries in NPG films can be potential active sites in the electrochemical reactions.

3.4. Electrochemical reaction of AA on NPG electrode

The implication of high structural defects, different grain sizes, and their anisotropic lattice orientations in the NPG film was studied on the electrochemical oxidation of AA. To observe the potential catalyzing effect of the NPG film, the AA electrooxidation was also investigated on a conventional gold disk electrode, which is devoid of structural defects. The voltammograms of bare and NPG-modified Au electrodes, recorded in 0.1 M PBS buffer solution containing 0.5 mM AA (Figure 6), show an oxidation peak in the forward scan, which corresponds to the oxidation of AA into dehydroascorbic acid (DHA) [25], while the absence of a reduction peak confirms the redox behavior of AA as irreversible. Notably, a big difference in both oxidation peaks´ shape, peak potential, and current can be observed. The anodic peak is broad, with high overpotential and low current when the voltammogram was recorded with the bare gold electrode, characteristic of slow electrochemical reactions. On the contrary, the NPG-modified Au electrode presents a much sharper oxidation peak, possessing twice higher current and a shift of 0.35 V toward less positive potentials compared to the bare gold electrode, indicating the electron transfer process is facilitated. Indeed, such a remarkable potential shift confirms the strong electrocatalytic effect of the NPG material. Thus, the surface and internal volume structure of the NPG film, possessing different orientations of grains, structural defects, and grain boundaries, make the electrooxidation of AA easier. Finally, the NPG´s increased electrochemical surface contributes to a higher oxidation current. However, enhancement in the current is only 2-fold despite much larger surface area of NPG, which is attributed to mass transport limitation of AA within the NPG porous volume [25, 50].

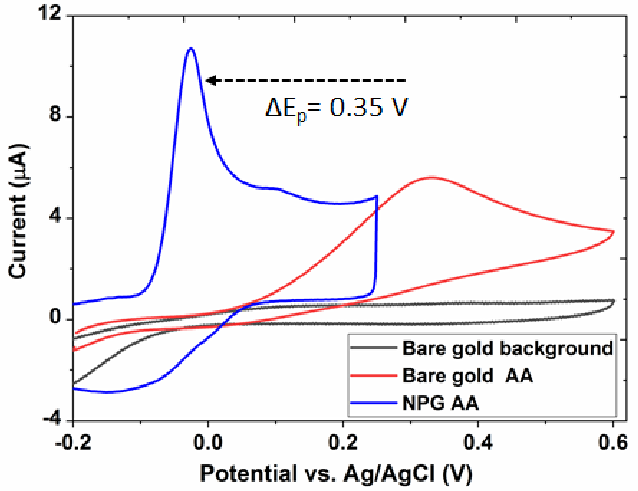

Figure 6: Comparison of voltammograms recorded with bare and NPG-modified Au electrodes in 0.1 M PBS+0.5 mM AA at a scan rate of 40 mVs^{-1}. The background CV is shown in black.

3.5. Computational studies of AA interaction on the active sites

One of the key difference in the structure of NPG film from the bare gold electrode is the presence of different orientations of grains, exposing multiple facets and grain boundaries, which are imparting a strong electrocatalytic effect for the AA oxidation. To understand the underlying mechanism, the interaction of AA on different Au facets and on grain boundaries were investigated by DFT calculations. For each facet, several initial adsorption structures are probed. The model structures have AA molecule with different orientations relative to the surface vectors on the slab, and probe different initial adsorption sites. we define the adsorption site as the position of the C atom connecting the oxolane-like ring and the tail structure in ascorbic acid in its final configuration as it would assume on the perfect surface. We select some characteristic adsorption sites depending on the facet. The choices include, for instance, top (T), bridge (B), hcp (H_x) hollow (H) and fcc (F) sites. In top panel of Figure 7, selected adsorption sites are indicated for each of the probed facets. Note that the top layer of Au atoms is shown in blue, 2nd layer in white, and deeper layers in shades of red. For the (111)/(100) interface, we show tested adsorption sites for different regions on the slab, i.e., a (111)-like as T_{111}, a (100)-like as T_{100}, and a disorder-like part as T_{dis}. The initial molecular arrangements on the surface were flat lying molecule with a distance of about 3.6 Å. The initial molecular orientations were, if applicable, adapted to the symmetry of the surface. We align the long axis of the molecule aligned parallel to one of the surface lattice vectors (assuming a surface spanning in *xy*-plane) and azimuthal rotated on (111) by 30°, whereas we used 0°, 45° and 90° azimuthal rotations for the other surfaces. In addition, the molecule was flipped/mirrored in the *xy*-plane, i.e. a polar rotation by π, for all azimuthal orientations and adsorption sites.

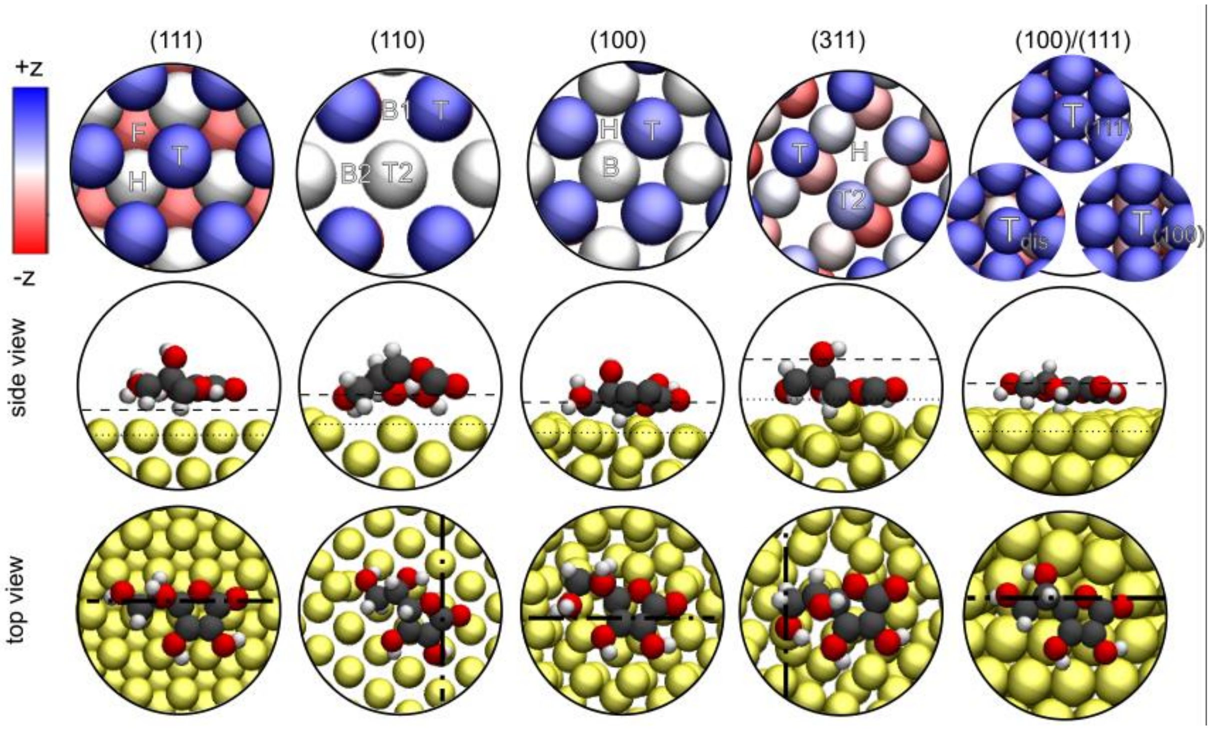

Figure 7: Probed adsorption sites (T: top at 1st layer (blue), B: bridge, H: hollow, H_x: hcp, F: fcc, T2: top 2nd layer (white), etc.) on different Au facets (top panel). DFT optimized AA structures on different Au facets. (from left to right): (111), (110), (100), (311), and (111)/(100) interface in side view (middle panel) and top view (lower panel). Atomic color code is H : white, C : brown, O : red, Au : yellow. Dashed and dotted lines assist the reader's eye in gauging positions between structures and $\Delta\rho$ (see Figure 9).

The most stable optimized structures of AA, i.e. those that minimize E_{ad}, on each facet are given in a side and top view in the middle and lower panel of Figure 7, respectively. The computed adsorption energies of AA on different Au facets are summarized in Table 1 for all molecular orientations. For each facet, only most exothermic results for a probed adsorption site are reported. The results show increasing binding strength between Au facet and the molecule in the order of (111) < (100) < (110) < (311). On those facets, the magnitude of binding strength ranges from -2.2 to -3.1 eV indicating exothermic processes. Moreover, the energy difference of adsorption sites Δ for a given facet is the smallest for the (111) case with a value of 60 meV, highlighting its inertness. Au (100) and Au (110) have larger Δ of about 250 meV, i.e. they display a stronger dependence on the adsorption site. Notably, the facets have minima (strongest binding) and maxima (weakest binding) at different adsorption sites. Thus, AA adsorbs on hollow sites for Au (100) and on bridge sites for Au (110). A larger Δ of ca. 500 meV is observed at (311) with the T as minimum and a T_2 as maximum. Only (311) shows a noticeable amount of surface reorganization during AA adsorption among the probed facets, such that Au atoms are being displaced (lateral and out-of-plane distortions) from their positions they assume in the pristine surface calculations. This indicates increased reactivity of AA on (311) facet of Au.

In the case of a grain boundary even stronger binding of AA was determined for the (111)/(100) interface (ca. 4 eV). The probable cause of this strong binding is the vacancy-like sites at the interface in the T_{dis} region with stronger reactivity. It is observed that one of the H atoms of AA occupies this space in the optimized geometry. Then, AA can overcome steric hindrance in the bond formation with Au atoms and simultaneously optimize the van der Waals (vdW) binding and local bond formation. In contrast to the (111) and the (100) systems, the (111)/(100) grain boundary displays Au surface atom reorganization upon AA adsorption, while appearing mostly in the surface plane, near the T_{dis} adsorption site. This is similar to the (311) case, indicating increased reactivity. For binding at T_{111} and T_{100} regions of the grain boundary, binding strength of -3.01 and -2.96 eV are observed, respectively. Those values are a few 100 meV larger than on their respective Au (111) and Au (100) facets, and are in the order of -3.0 eV, a value reached on rather reactive Au (311). This observation is attributed to strain within the grain boundary, which is also evidenced in the TKD characterization of the NPG film. Thus, the binding strength of AA on the grain boundary is increased compared to the other facet calculations. Since the effect was strongest for the disorder site (T_{dis}), and weaker for T_{111} and T_{100}, possible causes can likely be addressed to strain and disorder induced reactivity increased at the grain boundary.

Table 1. Adsorption energies of L-ascorbic acid on difference facets of Au surfaces. Values are given in eV. Configurations with strongest binding between molecule and a specific facet are highlighted in bold font.

	(100)	**(110)**	**(111)**	**(311)**	Grain interface (111)/(100)
T	-2.21	-2.57	-2.17	**-3.11**	
T2	-	-2.57	-	-2.55	**T_{100}:**
B1	-	**-2.77**	-	-	-2.96
					T_{111}:
B2	-	**-2.77**	-	-	-3.01
F	-2.27	**-**	-2.20		**T_{dis}:**
$H_{(x)}$	**-2.45**	-	**-2.23**	-2.69	**-3.97**
d_{ad} / Å	2.30	2.48	2.37	2.43	2.63
h / Å	2.14	2.42	2.01	2.42	0.89

d / Å	2.52	2.48	2.93	2.43	2.52
$\Delta\rho_I$ / e^-	-0.24	-0.28	-0.19	-0.24	-0.13 to -0.28

The atomic structure of the most stable adsorption configurations for different facets and the model of the grain interface are also investigated. The structures of the highlighted configurations given in Table 1 are presented in Figure 7. The L-ascorbic acid is non-planar molecule. Hence, possible adsorption structures of AA orient differently on adsorption sites on different facets. We classify the observed results into different cases using the alignment of the furan-like five-membered ring of AA and its functional groups (carbonyl (C=O), and ether (R-O-R') group) as well as the connected atomic chain with two hydroxyl groups on the surface. In the case of adsorption onto Au (111), (100) and (311), AA prefers an almost parallel furan-like ring, whereas the inner hydroxyl group of the atomic chain points away from the surface. Because the Au (111) is a closed packed surface and is rather inert, the molecule assumes a position where a H atom is closest to a surface atom (d_{ad} =2.4 Å), while the heavier elements have rather large distances of about $d = 3$ Å. The (110) and (100) facets offer space between surface atoms, allowing the molecule's hydroxyl group to face the substrate. On (110) substrate, the furan-like 5-membered ring is slightly tilted away from a parallel orientation. and the molecule is flipped, i.e. the inner hydroxyl group of the atomic chain points towards the surface. This leads to similar values of about 2.5 Å for the shortest binding distance between AA and Au for both, its H atoms (d_{ad}) and its heavier elements (d) on (110). The bond lengths of AA's H atom with Au take similar values for (100) and (311), i.e. 2.3 and 2.4 Å, respectively. On the other hand, the bonds formed between other atoms and Au are shorter than for (111), i.e. $d =$ 2.5 Å on (100) and (110), and 2.4 Å on (311), reflecting the increased interaction strength on those surfaces (in order: (111)<(100)<(110)<(311)). Furthermore a certain degree of structural flexibility and bending in AA on these surfaces are visualized, mainly noticeable at (100) and (110), as well as changes of the Au atom positions. For the grain boundary, the molecular plane arranges somewhat parallel to Au's surface and has a distance d_{ad} of about 2.6 Å, which is larger than Au (111). However, the d value is reduced from 2.9 A on (111) to 2.5 Å at the interface. Interestingly, the grain boundary shows the shortest distance between H atom and the Au top layer plane, resulting in a very short minimal height (h) of only 0.9 Å. This bond is formed to a Au atom in the 2nd Au layer. Therefore, strain and interaction with vacancy-like regions result in an increased reactivity, causing larger adsorption energy and decreased binding and adsorption distances at the grain boundaries compared to Au (111).

The charge transfer between AA and the Au facets was computed with the charge density difference profile as depicted in Figure 8. The charge transfer between molecule and substrate is computed through integration of $\Delta\rho$ from quasi-infinity above the molecule to the xy-plane of $\Delta\rho_{xy}$ between the molecule and substrate where $\Delta\rho_{xy} = 0$. The resulting charge transfer $\Delta\rho_l$ is given in e^-. Negative values indicate transfer of electrons from the molecule to the substrate and positive values indicate vice versa. In all cases AA transfers electronic charge to the Au surface, which is consistent with AA known as mild reducing agent.

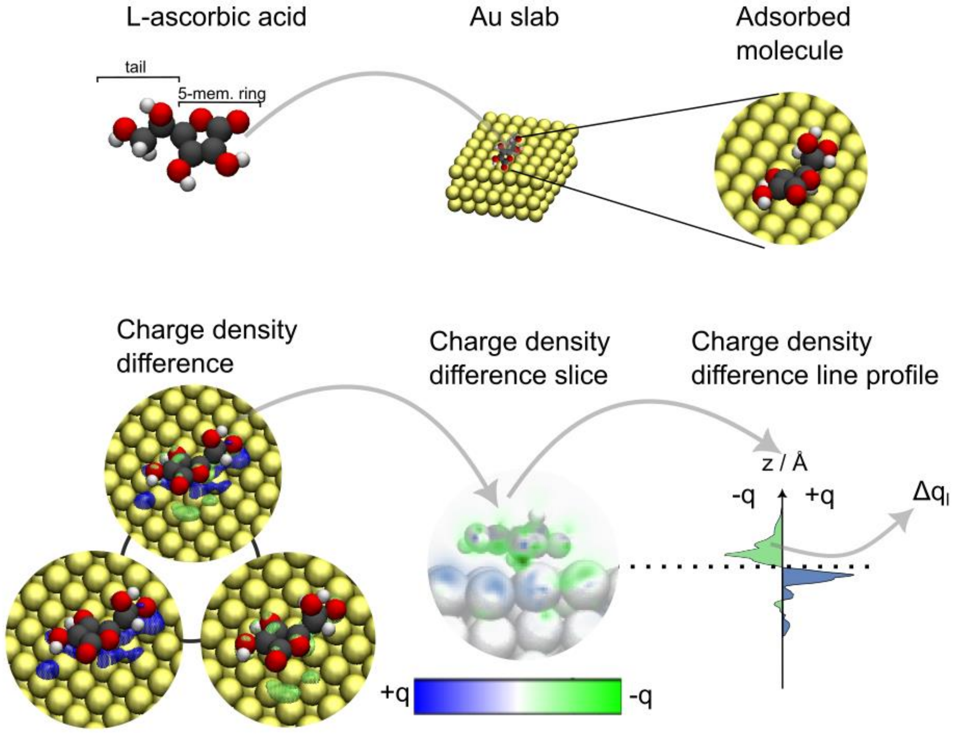

Figure 8. Procedure of computing the charge transfer. Top panel shows the optimized adsorption structure. Bottom panel determines the charge density difference (green regions as electron density depletion – blue areas as accumulation), the interface plane between molecule and metal surface, and integrate the charge transfer line profile over the molecule region yieldingΔq_1.

The data indicate stronger binding related to changes in the charge density at the molecule/Au interface, as shown in the $\Delta\rho$, $\Delta\rho$ slice and its line profile in Figure 9. To gauge positions between structure and $\Delta\rho$, dashed and dotted lines in Figure 7 and 9 relate to equivalent positions at the substrate and molecule, respectively. The orientation of $\Delta\rho$ slice is given as dashed-dotted line in Figure 7. The charge density changes appear near the hydroxyl groups on the tail and five-membered ring as accumulation of charge (i.e. blue isodensity contours) indicating some form of bond formation. Regions of charge depletion (i.e. green isodensity contours) are noticeable, too. The effect is weakest on (111) facet, and strongest for (110), while intermediate for (311) where noticeable changes occur at the ether and carbonyl groups. For the (100) case, $\Delta\rho$ is different by comparison. Most of the changes in the charge density are distributed at the tail region of the molecule. Hence, the changes occur in a rather delocalized way. The grain boundary case shows a stronger effect than on the (111) surface, but overall, as less than for the (100) case, i.e. scaled by a factor of 3.5, given in the $\Delta\rho$ slice. However, the positioning of one of the H atoms into a vacancy-like surface defect in the Au grain boundary results in formation of a strong $\Delta\rho$ in that region. This indicates localized bond formation possibly with partial covalent character. This is more similar to the (100) and (110) cases, where somewhat localized bonds are formed. The grain boundary case, therefore, benefits from presence of vdW and localized bonds that cause stronger binding.

The $\Delta\rho$ line profile gives in all cases a transfer of electronic charge to the substrate. Overall, the $\Delta\rho$ line profiles appear similar to each other that is a rather smooth appearance in the molecular region and some stronger fluctuations in the substrate region. The charge transfer values range from -0.13 to -0.28 e^-, i.e. transfer from the molecule to the substrateis seen in all cases. The smallest transfer values (given in Table 1) were found for the (111) case (-0.19 e^-) and at the grain boundary (-0.13 e^-). However, the latter case is affected by the mentioned H-atom occupying a vacancy-like defect. If the integration space of the line profile is partially extended for that region, an additional transfer of -0.15 electrons is estimated, i.e. a total of -0.28 e^-. Then, the value is comparable to the reactive (110) and (100) surface with transfer of -0.28 and -0.24 e^-, respectively.

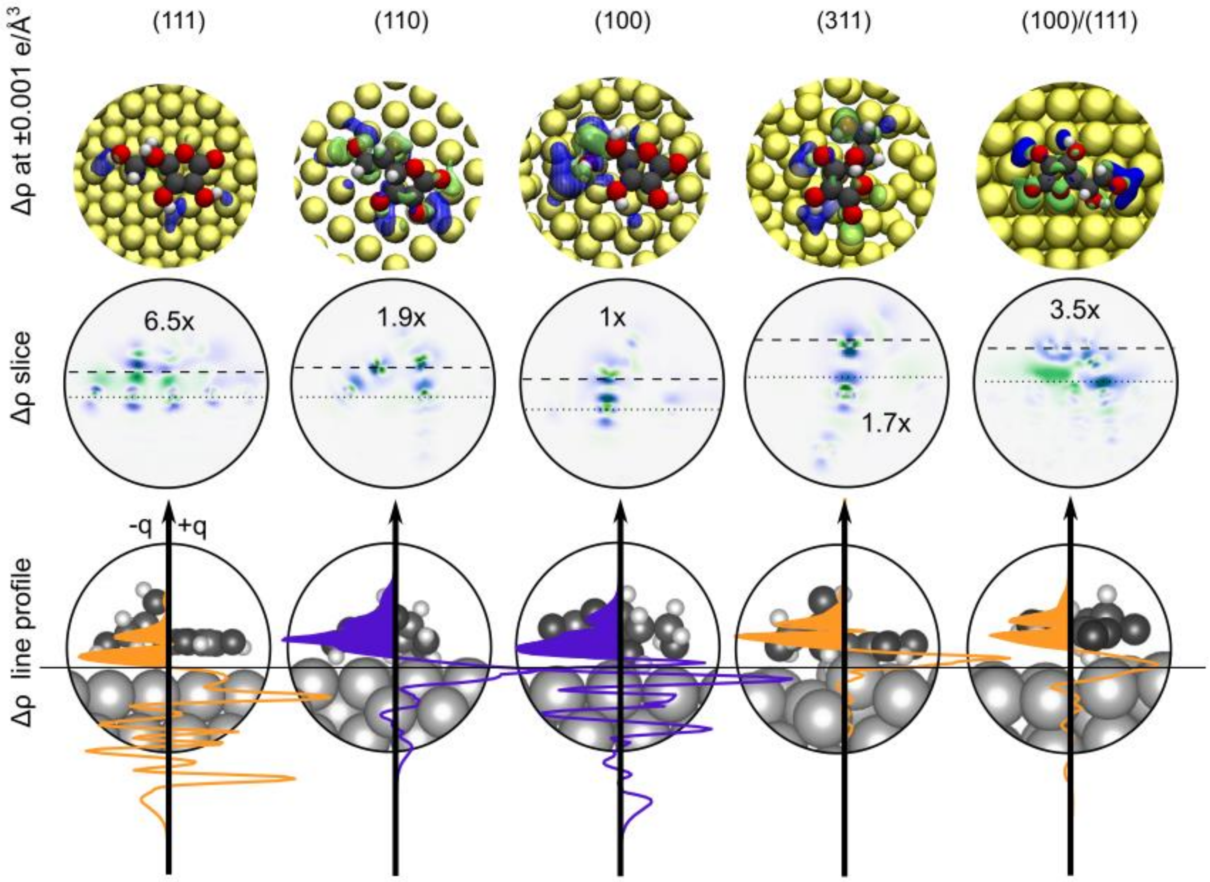

Figure 9: Top panel: Overview of charge density difference at different parts of AA ; middle panel: Scaled charge density slice; bottom panel: Charge transfer line profile for (left to right) (111), (110), (100), (311) and (100)/(111). Dashed and dotted lines assist the reader's eye in gauging positions (see Figure 7).

It is interesting to note that the different binding mechanisms of AA on Au seems to balance vdW interaction and local bond formation and depends on the facets. It results in favoured parallel orientation of molecular cycle parallel to the surface when vdW interactions dominate the attachment, in particular, the vdW interactions benefit from parallel alignment of the molecule with facets topography. The local bond formation can be stronger and impact the alignment of AA due to directional preferences. For the (111) and (100), the optimized structures show mostly flat-lying AA with furan-like rings almost parallel to the surface and parts of the tails point away from Au. These systems have rather large binding distance (d is about 2.5 Å on (100) and 2.9 Å on (111) and d_{ad} is ca. 2.3 Å), pointing to a vdW binding mechanism. AA on (100) shows a larger amount of charge transfer compared to (111), giving reason to the slightly larger binding strength. The larger binding strength in (110), (311) and the grain boundary cases is attributed to either local bond formation between AA and the surface resulting in small d_{ad}. Overall, the computational results reveal a facets dependence on the binding strength and mechanism (based on distances, energies, and charge transfer and charge density differences) of AA on Au. Generally, the binding is weak on the (111) which has a rather flat topography and is stronger on non-flat surfaces such as (311) or (110). Defects such as vacancies at grain boundary facets or strained region impact the adsorption behaviour and can lead to strong binding of AA.

Conclusions

In summary, we have clearly demonstrated the identification of intrinsic catalytic sites and unraveled their origin in the NPG film prepared by bottom-up DHBT approach. The microstructural characterizations by different electron microscopies revealed that evolution of low indexed crystalline grains, multiple grain boundaries and intra-grain structural defects are the potential sites to cause catalysis during the redox active species interaction. Microstructural orientation mapping of a thin slice of NPG film cross-section by Kikuchi diffraction pattern provides convincing evidence that faster kinetics of H_2 bubbles evolution during the Au atoms crystallization is the principal factor in inducing grain boundaries and structural defects in the NPG film. We also identified that NPG grains follow a unique growth pattern, such that in the beginning of the film growth, smaller sizes grains are formed near the substrate, making the region highly polycrystalline, while in the latter stage of film growth, larger grains with monocrystalline nature are developed. Therefore, within the NPG volume, grain sizes are bigger near the surface and are much smaller in the interior. Structural defects distribution within the NPG film is identified by GOS mapping, which highlights their higher proportion in the grains close to the surface of the NPG film. These structural defects are also directly visualized at the atomic scale by HRTEM imaging, showing many dislocations, steps and kinks in the NPG film. The NPG film displayed strong electrocatalytic behavior in the oxidation of AA, compared to bare gold electrode, inducing a 0.35 V cathodic shift of the AA overpotential. The DFT simulation confirmed that AA molecule undergoes preferential adsorption over the low index facets of Au and the grain boundaries, which are in abundance near the surface of the NPG film. In particular at the grain boundary, vacancy-like sites can form, in which part of AA fits to have a stronger interaction and forms a bond with partial covalent nature. The inert character of (111) plane is assigned to its flat topography over which charge transfer from AA is lower. The outcome of the present work will have a strong influence on microstructural designing of NPG catalysts to maximize its catalytic activities in the electrooxidation reactions. Investigating electrocatalysis of other antioxidants, such as gallic acid and caffeic acid on structurally engineered NPG electrodes and finally constructing an electroanalytical platform for selective determination of different antioxidants will be potential perspectives of our future activities.

Supporting Information

The supporting information contains following content;

Experimental details of surface area calculation, XRD of NPG film, SEM image of NPG film, XPS high resolution spectrum of NPG, TKD mapping of NPG and strain contour of NPG in the cross-section.

Acknowledgements

The authors acknowledge funding through Sao Paulo Research Foundation (FAPESP) through the projects (2014/50867-3), (2016/07461-1), (FAPESP 2018/16896-7) and (2018/08782-1). Authors thank PO FEDER-FSE Bourgogne 2019/2022 (via CoMICS program) and Agence Nationale de la Recherche (ANR) through the project OUTSMART (ANR-2015-CE39-0004-03) for funding. A.K. acknowledges financial support from MatElectroCap project (region Bourgogne Franche-Comté). J.L. thanks the National Science and Technology Council R.O.C for financial support under project 110-2112-M-110-025-MY3, the National Center for High-performance Computing (NCHC) of National Applied Research Laboratories (NARLabs) in Taiwan for providing computational and storage resources.

References

1. Bligaard, T.; Nørskov, J. K.; Dahl, S.; Matthiesen, J.; Christensen, C. H.; Sehested, J., The Brønsted–Evans–Polanyi Relation and the Volcano Curve in Heterogeneous Catalysis. *J. Catal.* **2004,** *224* (1), 206-217.

2. Sankar, M.; He, Q.; Engel, R. V.; Sainna, M. A.; Logsdail, A. J.; Roldan, A.; Willock, D. J.; Agarwal, N.; Kiely, C. J.; Hutchings, G. J., Role of the Support in Gold-Containing Nanoparticles as Heterogeneous Catalysts. *Chem. Rev.* **2020,** *120* (8), 3890-3938.

3. Ferraz, C. P.; Navarro-Jaén, S.; Rossi, L. M.; Dumeignil, F.; Ghazzal, M. N.; Wojcieszak, R., Enhancing the Activity of Gold Supported Catalysts by Oxide Coating: towards Efficient Oxidations. *Green Chem.* **2021,** *23* (21), 8453-8457.

4. Lopez, N.; Janssens, T. V. W.; Clausen, B. S.; Xu, Y.; Mavrikakis, M.; Bligaard, T.; Nørskov, J. K., On the Origin of the Catalytic Activity of Gold Nanoparticles for Low-temperature CO Oxidation. *J. Catal.* **2004,** *223* (1), 232-235.

5. Shang, C.; Liu, Z.-P., Origin and Activity of Gold Nanoparticles as Aerobic Oxidation Catalysts in Aqueous Solution. *J. Am. Chem. Soc.* **2011,** *133* (25), 9938-9947.

6. Boronat, M.; Leyva-Pérez, A.; Corma, A., Theoretical and Experimental Insights into the Origin of the Catalytic Activity of Subnanometric Gold Clusters: Attempts to Predict Reactivity with Clusters and Nanoparticles of Gold. *Acc. Chem. Res.* **2014,** *47* (3), 834-844.

7. Gonçalves, J. M.; Kumar, A.; da Silva, M. I.; Toma, H. E.; Martins, P. R.; Araki, K.; Bertotti, M.; Angnes, L., Nanoporous Gold-Based Materials for Electrochemical Energy Storage and Conversion. *Energy Technol.* **2021,** *9* (5), 2000927.

8. Lackmann, A.; Mahr, C.; Schowalter, M.; Fitzek, L.; Weissmüller, J.; Rosenauer, A.; Wittstock, A., A Comparative Study of Alcohol Oxidation over Nanoporous Gold in Gas and Liquid Phase. *J. Catal.* **2017,** *353*, 99-106.

9. Dou, J.; Tang, Y.; Nguyen, L.; Tong, X.; Thapa, P. S.; Tao, F. F., Oxidation of Cyclohexene Catalyzed by Nanoporous Au(Ag) in Liquid Phase. *Catal. Lett.* **2017,** *147* (2), 442-452.

10. Xu, C.; Su, J.; Xu, X.; Liu, P.; Zhao, H.; Tian, F.; Ding, Y., Low Temperature CO Oxidation over Unsupported Nanoporous Gold. *J. Am. Chem. Soc.* **2007,** *129* (1), 42-43.

11. Wittstock, G.; Bäumer, M.; Dononelli, W.; Klüner, T.; Lührs, L.; Mahr, C.; Moskaleva, L. V.; Oezaslan, M.; Risse, T.; Rosenauer, A.; Staubitz, A.; Weissmüller, J.; Wittstock, A., Nanoporous Gold: From Structure Evolution to Functional Properties in Catalysis and Electrochemistry. *Chem. Rev.* **2023,** *123* (10), 6716-6792.

12. Kumar, A.; Gonçalves, J. M.; Sukeri, A.; Araki, K.; Bertotti, M., Correlating Surface Growth of Nanoporous Gold with Electrodeposition Parameters to Optimize Amperometric Sensing of Nitrite. *Sens. Actuators B: Chem.* **2018,** *263*, 237-247.

13. Kumar, A.; Selva, J. S. G.; Gonçalves, J. M.; Araki, K.; Bertotti, M., Nanoporous Gold-Based Dopamine Sensor with Sensitivity Boosted by Interferant Ascorbic Acid. *Electrochim. Acta* **2019,** *322*, 134772.

14. Kumar, A.; Furtado, V. L.; Gonçalves, J. M.; Bannitz-Fernandes, R.; Netto, L. E. S.; Araki, K.; Bertotti, M., Amperometric Microsensor Based on Nanoporous Gold For Ascorbic Acid Detection in Highly Acidic Biological Extracts. *Anal. Chim. Acta* **2020,** *1095*, 61-70.

15. Downs, A. M.; Gerson, J.; Hossain, M. N.; Ploense, K.; Pham, M.; Kraatz, H.-B.; Kippin, T.; Plaxco, K. W., Nanoporous Gold for the Miniaturization of In Vivo Electrochemical Aptamer-Based Sensors. *ACS Sens.* **2021,** *6* (6), 2299-2306.

16. Nishio, K.; Masuda, H., Anodization of Gold in Oxalate Solution to Form a Nanoporous Black Film. *Angew. Chem., Int. Ed.* **2011,** *50* (7), 1603-1607.

17. Ding, Y.; Kim, Y. J.; Erlebacher, J., Nanoporous Gold Leaf: "Ancient Technology"/Advanced Material. *Adv. Mater.* **2004,** *16* (21), 1897-1900.

18. Nugraha, A. S.; Han, M.; Ashok, A.; Kang, Y.; Kim, J.; Alshehri, S. M.; Ahamad, T.; Bando, Y.; Yamauchi, Y., Synergistic Mesoporous Bimetallic Gold-Silver Nanoparticles: Synthesis, Structure, And Superior Electrocatalytic Activity. *Nano Energy* **2023,** *116*, 108770.

19. Cherevko, S.; Chung, C.-H., Direct Electrodeposition of Nanoporous Gold with Controlled Multimodal Pore Size Distribution. *Electrochem. Commun.* **2011,** *13* (1), 16-19.

20. Yang, X.-Y.; Chen, L.-H.; Li, Y.; Rooke, J. C.; Sanchez, C.; Su, B.-L., Hierarchically Porous Materials: Synthesis Strategies and Structure Design. *Chem. Soc. Rev.* **2017,** *46* (2), 481-558.

21. Fujita, T.; Guan, P.; McKenna, K.; Lang, X.; Hirata, A.; Zhang, L.; Tokunaga, T.; Arai, S.; Yamamoto, Y.; Tanaka, N.; Ishikawa, Y.; Asao, N.; Yamamoto, Y.; Erlebacher, J.; Chen, M., Atomic Origins of The High Catalytic Activity of Nanoporous Gold. *Nat. Mater.* **2012,** *11* (9), 775-780.

22. Biener, J.; Biener, M. M.; Madix, R. J.; Friend, C. M., Nanoporous Gold: Understanding the Origin of the Reactivity of a 21st Century Catalyst Made by Pre-Columbian Technology. *ACS Catal.* **2015,** *5* (11), 6263-6270.

23. Seo, M.; Chung, T. D., Nanoconfinement Effects in Electrochemical Reactions. *Curr. Opin. Electrochem.* **2019,** *13*, 47-54.

24. Daggumati, P.; Matharu, Z.; Seker, E., Effect of Nanoporous Gold Thin Film Morphology on Electrochemical DNA Sensing. *Anal. Chem.* **2015,** *87* (16), 8149-8156.

25. Kumar, A.; Bettinger, M. F.; Vibhu, V.; Bouvet, M.; Meunier-Prest, R., Correlation of Hierarchical Porosity in Nanoporous Gold with the Mass Transport of Electron Transfer-Coupled-Chemical Reactions. *J. Electroanal. Chem.* **2023,** *931*, 117186.

26. Wordsworth, J.; Benedetti, T. M.; Somerville, S. V.; Schuhmann, W.; Tilley, R. D.; Gooding, J. J., The Influence of Nanoconfinement on Electrocatalysis. *Angew. Chem. Int. Ed.* **2022,** *61* (28), e202200755.

27. Wordsworth, J.; Benedetti, T. M.; Alinezhad, A.; Tilley, R. D.; Edwards, M. A.; Schuhmann, W.; Gooding, J. J., The Importance of Nanoscale Confinement to Electrocatalytic Performance. *Chem. Sci.* **2020,** *11* (5), 1233-1240.

28. Moskaleva, L. V.; Röhe, S.; Wittstock, A.; Zielasek, V.; Klüner, T.; Neyman, K. M.; Bäumer, M., Silver Residues as a Possible Key to a Remarkable Oxidative Catalytic Activity of Nanoporous Gold. *Phys. Chem. Chem. Phys.* **2011,** *13* (10), 4529-4539.

29. Takale, B. S.; Feng, X.; Lu, Y.; Bao, M.; Jin, T.; Minato, T.; Yamamoto, Y., Unsupported Nanoporous Gold Catalyst for Chemoselective Hydrogenation Reactions under Low Pressure: Effect of Residual Silver on the Reaction. *J. Am. Chem. Soc.* **2016,** *138* (32), 10356-10364.

30. Mahr, C.; Kundu, P.; Lackmann, A.; Zanaga, D.; Thiel, K.; Schowalter, M.; Schwan, M.; Bals, S.; Wittstock, A.; Rosenauer, A., Quantitative Determination of Residual Silver Distribution in Nanoporous Gold and Its Influence on Structure and Catalytic Performance. *J. Catal.* **2017,** *352,* 52-58.

31. Yim, W.-L.; Nowitzki, T.; Necke, M.; Schnars, H.; Nickut, P.; Biener, J.; Biener, M. M.; Zielasek, V.; Al-Shamery, K.; Klüner, T.; Bäumer, M., Universal Phenomena of CO Adsorption on Gold Surfaces with Low-Coordinated Sites. *J. Phys. Chem. C* **2007,** *111* (1), 445-451.

32. Montemore, M. M.; Madix, R. J.; Kaxiras, E., How Does Nanoporous Gold Dissociate Molecular Oxygen? *J. Phys. Chem. C* **2016,** *120* (30), 16636-16640.

33. Wang, L.-C.; Personick, M. L.; Karakalos, S.; Fushimi, R.; Friend, C. M.; Madix, R. J., Active Sites for Methanol Partial Oxidation on Nanoporous Gold Catalysts. *J. Catal.* **2016,** *344,* 778-783.

34. Plowman, B. J.; Jones, L. A.; Bhargava, S. K., Building with Bubbles: The Formation of High Surface Area Honeycomb-Like Films Via Hydrogen Bubble Templated Electrodeposition. *Chem. Commun.* **2015,** *51* (21), 4331-4346.

35. Kumar, A.; Gonçalves, J. M.; Selva, J. S. G.; Araki, K.; Bertotti, M., Correlating Selective Electrocatalysis of Dopamine and Ascorbic Acid Electrooxidation at Nanoporous Gold Surfaces with Structural-Defects. *J. Electrochem. Soc.* **2019,** *166* (14), H704-H711.

36. Huan, T. N.; Ganesh, T.; Kim, K. S.; Kim, S.; Han, S.-H.; Chung, H., A Three-dimensional Gold Nanodendrite Network Porous Structure and Its Application For an Electrochemical Sensing. *Biosens. Bioelectron.* **2011,** *27* (1), 183-186.

37. Hernández-Saravia, L. P.; Sukeri, A.; Bertotti, M., Fabrication of Nanoporous Gold-Islands Via Hydrogen Bubble Template: An Efficient Electrocatalyst for Oxygen Reduction and Hydrogen Evolution Reactions. *Int. J. Hydrogen Energy* **2019,** *44* (29), 15001-15008.

38. Hussein, H. E. M.; Maurer, R. J.; Amari, H.; Peters, J. J. P.; Meng, L.; Beanland, R.; Newton, M. E.; Macpherson, J. V., Tracking Metal Electrodeposition Dynamics from Nucleation and Growth of a Single Atom to a Crystalline Nanoparticle. *ACS Nano* **2018,** *12* (7), 7388-7396.

39. Hohenberg, P.; Kohn, W., Inhomogeneous Electron Gas. *Phys. Rev.* **1964,** *136* (3B), B864-B871.

40. Kohn, W.; Sham, L. J., Self-Consistent Equations Including Exchange and Correlation Effects. *Phys. Rev.* **1965,** *140* (4A), A1133-A1138.

41. Giannozzi, P.; Andreussi, O.; Brumme, T.; Bunau, O.; Buongiorno Nardelli, M.; Calandra, M.; Car, R.; Cavazzoni, C.; et al., Advanced Capabilities for Materials Modelling with Quantum ESPRESSO. *J. Phys.: Condens. Matter* **2017,** *29* (46), 465901.

42. Perdew, J. P.; Burke, K.; Ernzerhof, M., Generalized Gradient Approximation Made Simple. *Phys. Rev. Lett.* **1996,** *77* (18), 3865-3868.

43. Grimme, S., Semiempirical GGA-type Density Functional Constructed with a Long-Range Dispersion Correction. *J. Comput. Chem.* **2006,** *27* (15), 1787-1799.

44. Lüder, J.; Sanyal, B.; Eriksson, O.; Puglia, C.; Brena, B., Comparison of van der Waals Corrected and Sparse-Matter Density Functionals for the Metal-Free Phthalocyanine/Gold Interface. *Phys. Rev. B* **2014,** *89* (4), 045416.

45. Hamelin, A., Cyclic Voltammetry at Gold Single-Crystal Surfaces. Part 1. Behaviour at Low-index Faces. *J. Electroanal. Chem.* **1996,** *407* (1), 1-11.

46. Khristosov, M. K.; Bloch, L.; Burghammer, M.; Kauffmann, Y.; Katsman, A.; Pokroy, B., Sponge-like Nanoporous Single Crystals of Gold. *Nat. Commun.* **2015,** *6* (1), 8841.

47. Sylvestre, J.-P.; Poulin, S.; Kabashin, A. V.; Sacher, E.; Meunier, M.; Luong, J. H. T., Surface Chemistry of Gold Nanoparticles Produced by Laser Ablation in Aqueous Media. *J. Phys. Chem. B* **2004,** *108* (43), 16864-16869.

48. Feng, X.; Jiang, K.; Fan, S.; Kanan, M. W., Grain-Boundary-Dependent CO_2 Electroreduction Activity. *J. Am. Chem. Soc.* **2015,** *137* (14), 4606-4609.

49. Su, D.; Dou, S.; Wang, G., Gold Nanocrystals with Variable Index Facets as Highly Effective Cathode Catalysts for Lithium–Oxygen Batteries. *NPG Asia Mater*. **2015,** *7* (1), e155-e155.

50. Kumar, A.; Gonçalves, J. M.; Furtado, V. L.; Araki, K.; Angnes, L.; Bouvet, M.; Bertotti, M.; Meunier-Prest, R., Mass Transport in Nanoporous Gold and Correlation with Surface Pores for EC_1 Mechanism: Case of Ascorbic Acid. *ChemElectroChem* ***2021****, 8, 2129–2136*